Measuring Depth: Temporal Light Coding

Quote.

Author

1. DEPTH FROM TIME-OF-FLIGHT

In this chapter, we discuss techniques that use temporally coded light sources for recovering scene depths. The light source is modeled as a point source whose intensity can be modulated over time, typically at high speeds. Some examples of such light sources are laser diodes that emit light pulses of short duration (few picoseconds to a few nanoseconds) and light emitting diodes (LEDs) whose intensity can be modulated continuously over time at high frequencies (e.g., tens of MHz. to GHz.).

The depth measurement principle employed by these methods is time-of-flight (ToF), which can be explained as follows. Consider two points A and B in space such that the distance between them is d. Suppose an entity (a physical object or a wave) travels from A to B at a constant speed c. Let t be the time taken to travel between the two points. Then, d, c and t are related by the simple equation:

$$d = c \times t. \tag{1}$$

If the speed and travel time are known, the distance can be estimated. ToF as a distance measurement technique is used extensively in nature by animals such as bats and whales for navigation and hunting. These natural ToF systems are based on the propagation of sound waves.
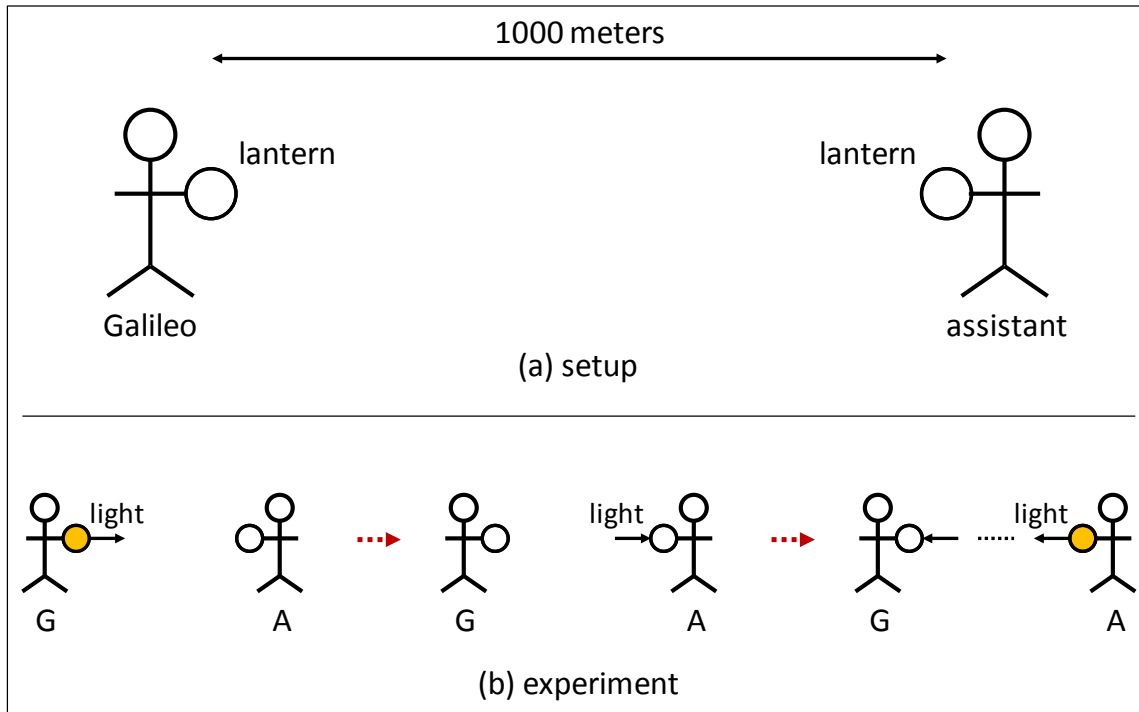
Fig. 1. **Galileo's experiment for establishing that light has a finite speed (**1638**).**

In this chapter, we will focus on light based, or optical ToF systems which use the known speed of light for estimating scene distances (depths).

1.1. Measuring The Speed Of Light

Galileo's Experiment. Till early 17th century, it was largely believed that light propagates instantaneously, i.e., it has infinite speed. Galileo Galilei was one of the first to believe that light has a finite speed. In 1638, he conducted a simple experiment to prove this. He positioned himself and an assistant on two hill-tops approximately 1000 meters apart. Each of them held a shuttered lantern, as illustrated in Figure 1. The experiment proceeded as follows. First, Galileo removed the shutter from his lantern so that it emits light. The assistant was instructed to remove his lantern's shutter as soon as he saw light from Galileo's lantern. The light from the assistant's lantern would then travel to Galileo. Galileo hoped to notice a time delay between the instant he uncovered his lantern and the instant he saw light from the other lantern, thereby establishing that light has a finite speed. Unfortunately, since there were no sophisticated timing instruments available, Galileo relied on his reaction time for experiencing the delay. We now know that light would have taken only about 6.6
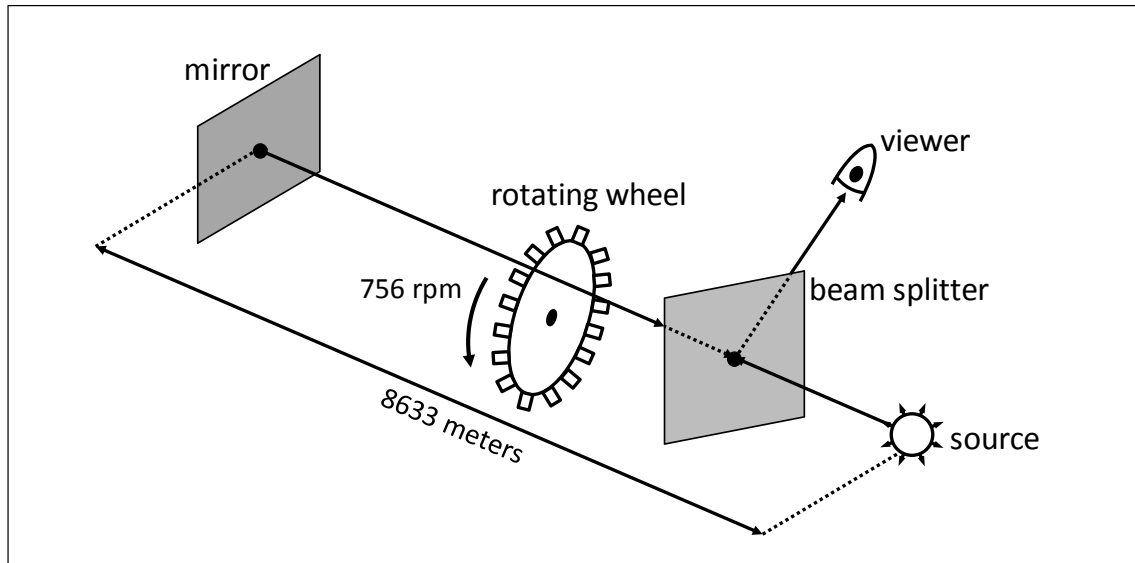
Fig. 2. **Fizeau's experiment to measure the speed of light (**1849**).**

microseconds to travel back and forth, which is significantly lower than human reaction times. Thus, he was not able to conclusively show that light has a finite speed.

Fizeau's Experiment. Around the year 1670, Danish astronomer Ole Roemer was observing the eclipses of Io, a moon of the planet Jupiter. While making timing measurements of the eclipses over the period of a few years, he observed some discrepancies, which he showed to be the result of light having a finite speed. However, he could not measure the speed of light accurately by using this phenomenon.

It was nearly 200 years later, in 1849, when Hippolyte Fizeau, a French physicist was able to measure the speed of light with an ingeniously designed experiment. The setup consisted of a collimated light source and a mirror placed at a distance of $d = 8633$ meters from each other. Since precise timing instruments were still not available at the time, it was not possible to estimate the speed of light directly by measuring the travel time between the light source and the mirror. Instead, Fizeau placed a toothed wheel between the source and the mirror, as shown in Figure 2. The wheel could rotate along its axis (along the line joining the source and the mirror). If the wheel rotated slowly, the light passing through the notch between two adjacent teeth would get reflected from the mirror, and come back through the same notch. This reflected light could be observed by a viewer via a beam-splitter. Next, the rotation speed of the wheel was increased so that the time taken by the wheel to rotate from a notch to the adjacent tooth became equal to the time taken by

the light to travel from the wheel to the mirror and back. In this case, the light that passes through a notch would get blocked on its return path by the adjacent tooth, and the viewer would not observe any light.

Let the rotation speed of the wheel when light is blocked is ν rotations per second, and the number of teeth in the wheel is N_{teeth}. Then, the time t taken by the wheel to rotate between one notch to the adjacent tooth is given by [1]:

$$t = \frac{1}{2\nu N_{teeth}} \,.$$
(2)

The estimated velocity $\hat{c}$ of the light is then given by:

$$\hat{c} = \frac{2d}{t} = 4d\nu N_{teeth} \,.$$
(3)

In Fizeau's setup, N_{teeth} and ν were approximately 750 and 12.6 rotations per second, respectively. Substituting the values in the above equation, we get the speed of light estimated by Fizeau, $\hat{c} \approx 3.13 \times 10^8$ meters per second. Remarkably, this value, obtained with a simple setup, is within 5% of the true speed of light.

Modern Measurement Methods. Currently, the speed of light is estimated by measuring the frequency and wavelength of frequency stabilized lasers [Evenson et al. 1972]. Since the year 1983, the speed of light has been fixed at $c = 2.99792458 \times 10^8$ meters per second. This measurement technique is considered sufficiently precise to be used for defining meter as the distance traveled by light in $\frac{1}{2.99792458 \times 10^8}$ of a second.

1.2. Optical ToF Based Depth Measurement Systems

Conceptually, all optical ToF systems have the same configuration and operation principle, as illustrated in Figure 3. They consist of a light source that emits temporally coded light, i.e., the intensity of the emitted light is temporally modulated. The light travels to the scene of interest, is reflected, and is captured by a sensor that is typically co-located with the light source. The total time taken by light to travel back and forth is measured by comparing the emitted light and the received light (at the sensor). Then, since the speed of light is known, Eq. 1 is used to estimate the scene depths.

---

[1]The notches and the teeth are assumed to have equal width, so that the time taken for the wheel to rotate from a notch to the tooth is half the time taken to rotate between two adjacent teeth.
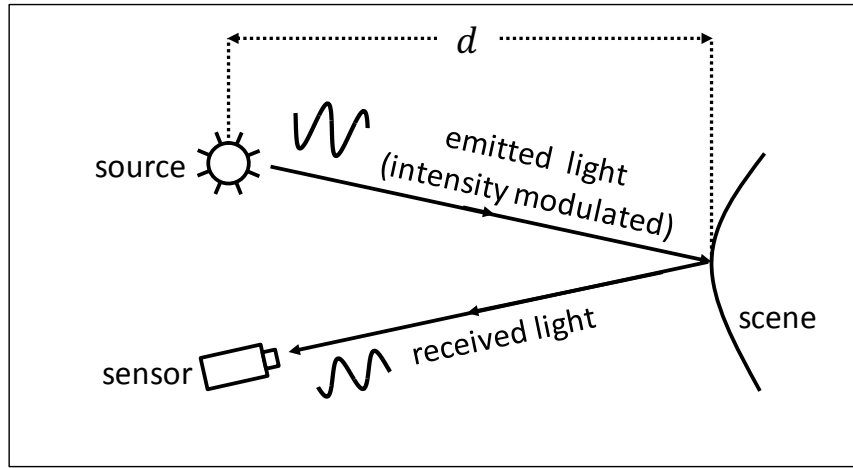
Fig. 3. **Basic configuration and operating principle of optical ToF based depth measurement systems.** Optical ToF systems consist of a light source that emits light whose intensity is temporally modulated. The light travels to the scene of interest, is reflected, and is captured by a sensor that is co-located with the light source. The total time taken by light to travel back and forth is measured by comparing the emitted light and the received light (at the sensor). The travel time is then used to estimate the scene depths.

The main difference between different ToF techniques is in the way the emitted light is modulated. Depending on the modulation signal used, optical ToF techniques can be broadly classified into two main categories:

— Impulse ToF
— Continuous-Wave ToF

In impulse ToF methods, the light source emits very short (typical duration of less than 1 nanosecond) pulses of light, whereas in continuous-wave (CW) ToF, the source emits light continuously with the intensity of light being continuously modulated over time. In the following, we will describe these approaches in detail.

2. IMPULSE TIME-OF-FLIGHT

Conceptually, the simplest ToF based depth recovery technique is impulse (or pulsed) ToF. An impulse ToF system consists of a light source emitting a short temporal pulse of light towards the scene to be measured. The pulse travels to the scene, and a fraction of it gets reflected in the direction of the sensor (detector). This is shown in Figure 4. In practice, the light source and the
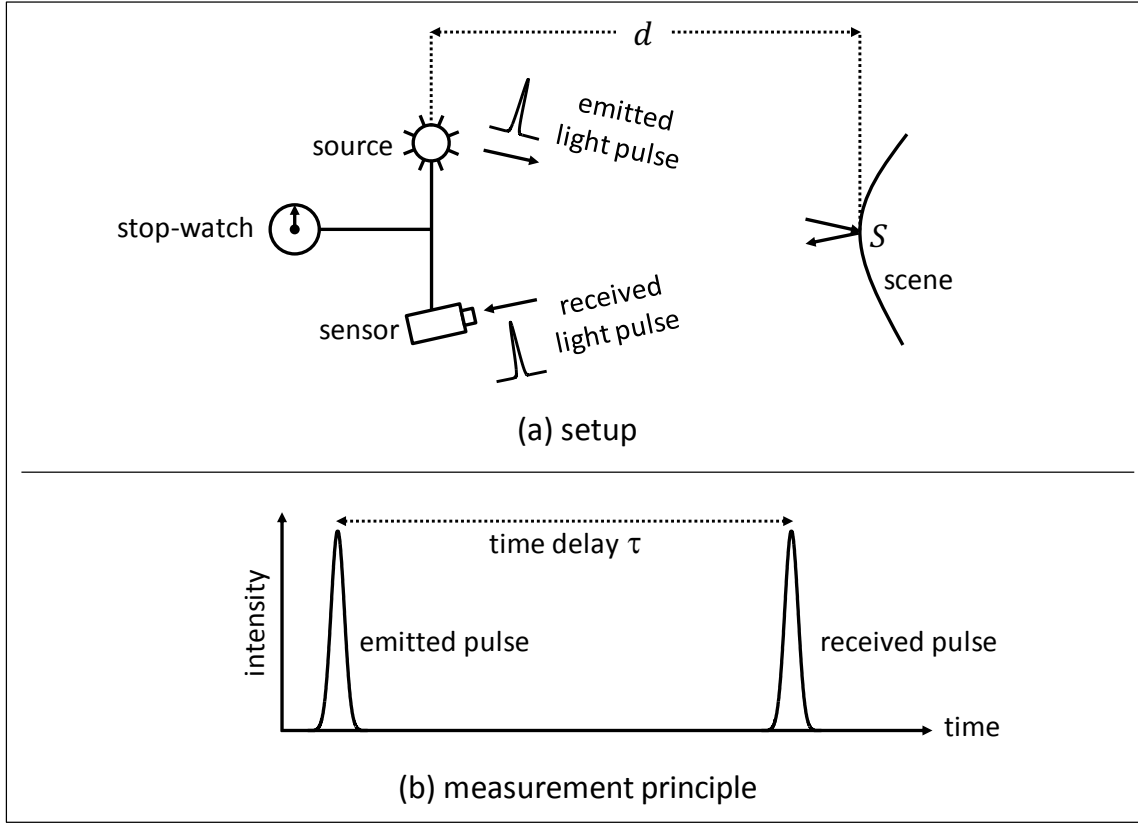
Fig. 4. **Impulse time-of-flight imaging.** Impulse ToF systems consist of a light source which emits short temporal pulses of light towards the scene to be measured. The pulse travels to the scene, and a fraction of it gets reflected in the direction of the sensor (detector). The source and the sensor are temporally synchronized so that they share the timing information. A high precision "stop-watch" measures the total travel time of the pulse - the time between when it is emitted by the source and when it is received by the sensor. The travel time is then used to estimate the scene depth.

sensor are located sufficiently close to each other so that they are assumed to be at the same 3D location in space [2].

Let t_{start} be the time instant when the source emits the pulse, and t_{stop} be the time instant when the sensor receives the pulse. The source and the sensor are temporally synchronized so that they share the timing information. A high precision "stop-watch" measures the total travel time

---

[2] Since the light source and sensor are located at the same 3D location, ToF based systems avoid the missing parts problem inherent in triangulation based depth recovery methods, as discussed in previous chapter (Section **??**).

$\tau = t_{stop} - t_{start}$, as illustrated in Figure 4. The distance d between the sensor and the scene is given by:

$$d = \frac{c\tau}{2} \,, \tag{4}$$

where c is the known speed of light. The factor of 2 on the right hand side accounts for the fact that the travel time τ is for round-trip distance.

Impulse ToF formed the basis of the first LIDAR (light-detection-and-ranging) systems nearly 50 years ago [Koechner 1968]. Since then, these systems have been widely used for measuring shape and position of objects, specially in applications involving large scale scenes such as architectural surveying, urban mapping, autonomous navigation, and inspection of aeroplanes and ships. LIDAR systems have also been used to capture large scale terrain data [Mamon et al. 1978]. Example topographic and bathymetric data for the United States is available for download from the United States Interagency Elevation Inventory [Administration]. Several commercial ToF based ranging systems are based on the impulse ToF technique [Velodyne ; Leica-Geosystems].

2.1. Hardware Implementation

An impulse ToF system has three main components: the source (transmitter), the sensor (receiver), and the timing unit (stop-watch).

Source. The source typically consists of a pulsed laser. Short optical pulses are generated by either driving the laser with an external electronics circuit, or by using mode-locked or Q-switched lasers.

Sensor. The sensor in an impulse ToF system converts the received optical pulse into an electrical pulse. Due to their low cost and size, photo-diodes are typically used as sensors [Moring et al. 1989], although in some implementations, photo-multiplier tubes have also been used [Koechner 1968]. Single photon avalanche photo-diodes (SPAD) are used in applications where higher sensitivity and precision is required [Cova et al. 1981; Massa et al. 1998].

Timing Unit. The time measurement unit or the stop watch is implemented with a time-to-amplitude-converter (TAC) or a time-to-digital-converter (TDC). The source and the sensor send electrical pulses to the time measurement unit at the instants when they emit and receive optical pulses. Let the source and sensor electrical pulses be called the start and stop pulse, respectively. A TAC produces an analog voltage that is proportional to the time delay between the start and the stop pulses. The analog voltage is measured after converting into a digital value. A TDC measures
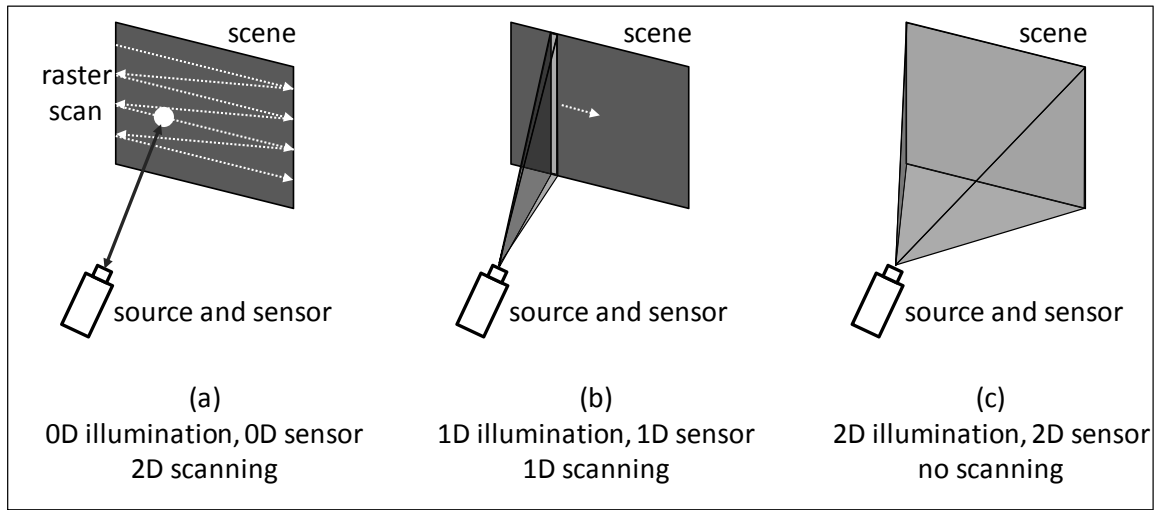
Fig. 5. **Different hardware setups for impulse ToF imaging.** (a) Point scanning systems emit a single beam of light and the detector is a single photo-diode. These systems measure the depth of a single scene point at a time. In order to measure the depth of an entire scene, the source and the sensor are moved along two dimensions. (b) Stripe scanning systems emit a 1D light sheet and the sensor consists of a 1D array of photo-diodes. Such a system requires scanning along one dimension. (c) A full-frame system consists of a 2D array of photo-diodes and a light source that emits an uncollimated light beam (e.g., a light cone). Such a system does not require any mechanical scanning.

the number of system clock periods between the two pulses. The higher the clock frequency, higher the temporal resolution of the TDC. For further details on hardware implementation of an impulse ToF system, see [Kilpela 2004].

2.2. Scanning Vs. Full-Frame Systems

In initial impulse ToF systems, the source emitted a single beam of light and the detector was a single photo-diode. These systems were single-point range systems, as they measured the depth of a single scene point at a time. In order to measure the depth of an entire scene, the source and the sensor were moved along two dimensions, requiring a large acquisition time. This is illustrated in Figure 5. Faster acquisition can be achieved by a source emitting a 1D light sheet and a 1D array of photo-diodes. Such a system requires scanning along one dimension [Velodyne]. A full-frame system can be achieved by using a 2D array of photo-diodes and a light source that emits an uncollimated light beam (e.g., a light cone) [Niclass et al. 2005]. Such a system does not require any mechanical scanning.

2.3. Noise And Error Analysis

There are several sources of noise in an impulse ToF system, including photon noise, sensor read noise, laser speckle, and the timing jitter in the timing unit. For instance, photon noise (due to the reflected light as well as ambient light sources) may cause spurious pulses in the received signal. This will produce incorrect measurement of the time delay τ. Let $\triangle \tau$ be the error in the delay measurement due to various noise sources. The resulting distance error $\triangle d$ is given by:

$$\triangle d = \frac{c \triangle \tau}{2} \,.$$
(5)

For instance, a timing error of 1 nanosecond will result in a distance error of 15 centimeters. For an extended noise analysis and a discussion of the noise sources in an impulse ToF system, see [Moring et al. 1989; Kilpela 2004].

Related papers: Impulse ToF systems have been used for measuring scene characteristics (3D shape, motion and appearance) of non-line-of-sight scenes ("around-the-corner") [Kirmani et al. 2009; Velten et al. 2012; Pandharkar et al. 2011]. These systems require very high timing resolution. Thus, they use mode-locked lasers with femto second pulse widths, and streak cameras with picosecond resolution.

3. CONTINUOUS-WAVE TIME-OF-FLIGHT

The major drawback of impulse ToF systems is the expensive hardware requirements. In order to achieve a high depth resolution, the laser source must emit pulses of very short durations (typically less than 1 nanosecond) and high optical power. The sensor needs to measure the light incident on it at a fast rate in order to detect the short returning pulses, thus requiring a high bandwidth. The timing unit must also have a high temporal resolution. For instance, in order to have a depth resolution of 1 centimeter, the timing of the received pulse must be resolved to within 66 picoseconds. These requirements significantly increase the cost of impulse ToF systems, often making them unsuitable for consumer applications.

In order to address these limitations, continuous-wave time-of-flight (CW ToF) systems were proposed [Payne 1973; Smith 1980]. A CW ToF imaging system consists of a light source whose intensity is continuously modulated over time. Such continuous modulation can be achieved on a wide range of light sources such as light emitting diodes (LEDs), which are significantly cheaper as

compared to lasers. Also, the sensor need not sample the incident radiance at high speeds, thus lowering the bandwidth requirements and cost of the sensor.

In CW ToF systems, the intensity of the source is modulated according to a continuous periodic function $M(t)$, called the modulation function. One of the most widely used modulation functions in CW ToF sensors is a temporal sinusoid. In this case, the radiant intensity emitted by the light source is given by [3]:

$$M(t) = o_m + a_m \cos(\omega t), \tag{6}$$

where o_m and a_m are the offset and the amplitude of the sinusoid. Since light intensity is always positive, $o_m \geq a_m$. Typically, $o_m = a_m$ in order to achieve the maximum intensity contrast.

As the emitted light travels to the scene and is reflected back to the sensor (assumed to be co-located with the light source), the sinusoid undergoes a temporal shift. Consider a scene point S, which is imaged at sensor pixel $\mathbf{p}$. The radiance $L(\mathbf{p}, t)$ incident at $\mathbf{p}$ is given by:

$$L(\mathbf{p}, t) = \alpha(\mathbf{p}) M\left(t - \tau(\mathbf{p})\right) + A(\mathbf{p}), \tag{7}$$

where $\tau(\mathbf{p}) = \frac{2d(\mathbf{p})}{c}$ is the temporal shift; it is the time taken by the light to travel from the source to scene point S, and then back to the sensor. $d(\mathbf{p})$ is the distance between the sensor and the scene point S. The constant $\alpha(\mathbf{p})$ encapsulates the reflectance properties and orientation of S, camera's gain, light source's brightness, and intensity fall-off. $A(\mathbf{p})$ is the ambient illumination term. It is assumed to be constant over time [4]. After substituting Eq. 6 into Eq. 7, and simplifying, we get:

$$L(\mathbf{p}, t) = o_l(\mathbf{p}) + a_l(\mathbf{p}) \cos\left(\omega t - \phi(\mathbf{p})\right), \tag{8}$$

where $o_l(\mathbf{p}) = \alpha(\mathbf{p}) o_l + A(\mathbf{p})$ and $a_r(\mathbf{p}) = \alpha(\mathbf{p}) a_l$. $L(\mathbf{p}, t)$ is also a temporal sinusoid with offset o_c, amplitude a_c and phase $\phi(\mathbf{p}) = \frac{2\omega d(\mathbf{p})}{c}$. Essentially, $L(\mathbf{p}, t)$ is a phase-shifted and scaled version of the emitted sinusoid $I(t)$. The amount of phase-shift, $\phi(\mathbf{p}) = \frac{2\omega d(\mathbf{p})}{c}$ is directly proportional to the scene depth, as shown in Figure 6.

---

[3]For ease of exposition, we assume the light source to be isotropic, that is radiating equal intensity in all directions

[4]In practice, $A(\mathbf{p})$ may vary over time. However, for most real-world scenarios, the temporal frequency of $A(\mathbf{p})$ is significantly lower than the temporal frequency of $M(t)$.
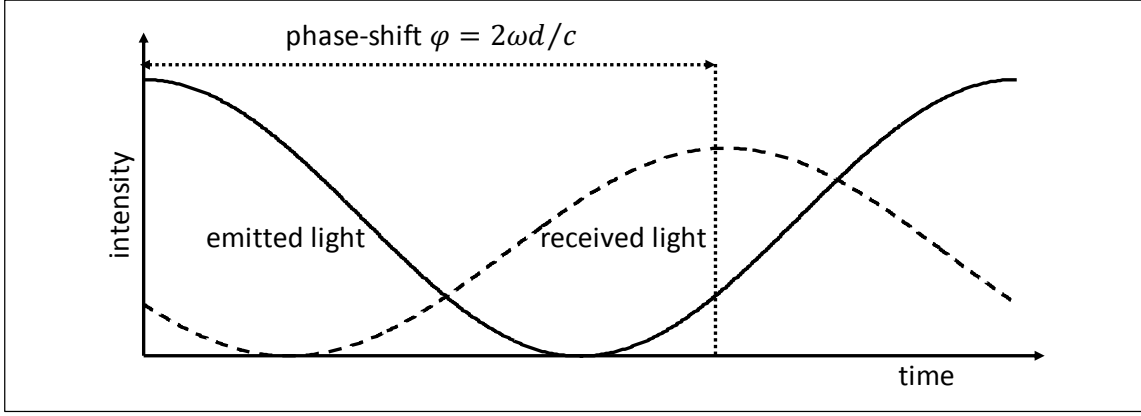
Fig. 6. **Basic principle of continuous wave ToF imaging.** In continuous-wave ToF systems, the intensity of the source is modulated over time according to a continuous periodic function. If the function is a sinusoid, the intensity of the emitted light varies temporally as a sinusoid. As light travels to the scene and is reflected back to the sensor, the phase of the sinusoid changes. The intensity of light received at the sensor also varies as a sinusoid, but with a different phase as compared to the emitted light. The difference in the phases of the emitted light and the received light is proportional to the travel time, and hence, the distance. Scene depths are computed by comparing the emitted and received light, and estimating their phase difference.

In order to measure the depth $d(\mathbf{p})$, the phase $\phi(\mathbf{p})$ needs to be estimated. The process of estimating phase (and hence depth) from the received radiance $L(\mathbf{p}, t)$ is called decoding or demodulation. As we will show shortly, in CW ToF techniques, decoding is performed by measuring the temporal correlation of the received radiance $L(\mathbf{p}, t)$ with a decoding function $R(t)$ (also known as demodulation function).

In CW ToF systems that use sinusoidal modulation of the light source, there are two main decoding approaches depending on the choice of the demodulation function $R(t)$ - homodyne decoding (modulation and demodulation functions, $M(t)$ and $R(t)$, are both sinusoids of the same temporal frequency), and heterodyne decoding ($M(t)$ and $R(t)$ are sinusoids of different frequency).

3.1. Homodyne Decoding

In homodyne decoding [Lange 2000], the demodulation function $R(t)$ is also a sinusoid of the same frequency ω as the source modulation function $M(t)$:

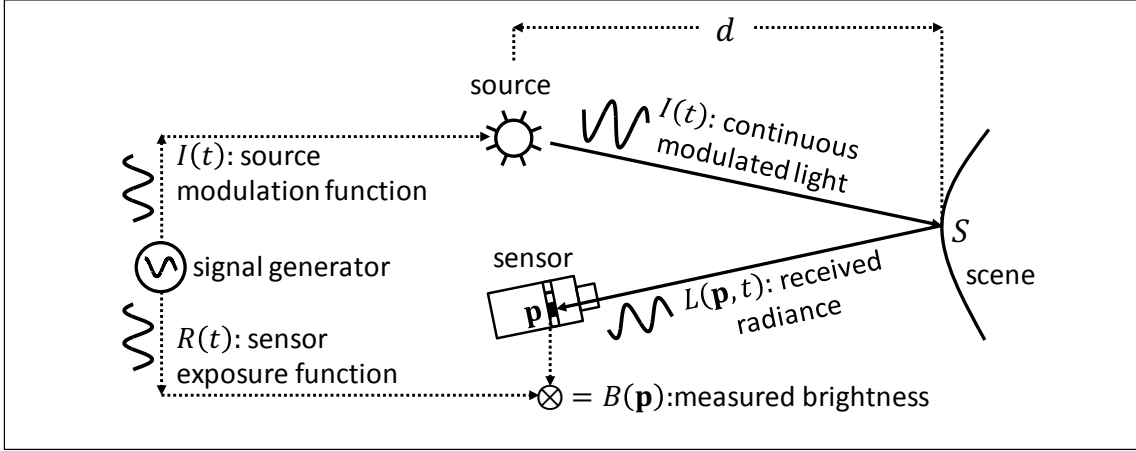$$R(\psi, t) = o_r + a_r \cos(\omega t - \psi), \tag{9}$$

Fig. 7. **Measuring phase of received light by taking correlation measurements.** In order to estimate the phase of the light received at the sensor, it is correlated (temporally) with a demodulation function. This is achieved by temporally modulating the the sensor's exposure according to the demodulation function. The measured brightness at a camera pixel is given as the correlation between the temporally varying incident radiance and the demodulation function.

where o_r and a_r are the offset and the amplitude of the demodulation function sinusoid. ψ is the relative phase between $R(t)$ and $M(t)$. In order to perform decoding, the sensor's exposure is temporally modulated during integration time according to $R(\psi, t)$ [5]. Then, the measured brightness $B(\mathbf{p}, \psi)$ at a sensor pixel $\mathbf{p}$ is given by the correlation between $R(\psi, t)$ and $L(\mathbf{p}, t)$:

$$
\begin{aligned}
B(\mathbf{p}, \psi) &= R(\psi, t) \star L(\mathbf{p}, t) \\
&= \int_{T-\frac{T_{int}}{2}}^{T+\frac{T_{int}}{2}} R(\psi, t) L(\mathbf{p}, t) dt,
\end{aligned}
\tag{10}
$$

where $\star$ is the correlation operator, T is the time instant at the middle of the sensor integration period, and T_{int} is the length of the integration period [6]. This is illustrated in Figure 7. Substituting Eqs. 8 and 9 in Eq. 10, and simplifying, we get:

---

[5]This can be achieved either by modulating the brightness gain of the sensor on-chip (e.g., photonic mixer devices [Schwarte et al. 1997; Lange 2000; Lange and Seitz 2001]) or by using fast optical shutters in front of the sensor [Anthes et al. 1993; Carnegie et al. 2011].

[6]The sensor integration period T_{int} can be significantly larger than the period of the modulation functions. For example, T_{int} could be 100 milliseconds, whereas the modulation and demodulation functions could be sinusoids with periods of 100 nanoseconds (modulation frequency $\omega = 10$ MHz.). Since the correlation is computed over large integration periods, the sensor need not sample the incident radiance at high speeds, thus lowering the bandwidth requirements and cost

$$B(\mathbf{p}, \psi) = o_b + a_b \cos\left(\psi - \phi(\mathbf{p})\right), \tag{11}$$

where $o_b = o_r o_l T_{int}$ and $a_b = \frac{a_r a_l T_{int}}{2}$ [7].

The above equation states that the measured brightness $B(\mathbf{p}, \psi)$ is also a sinusoidal function with three unknowns o_b, a_b, and $\phi(\mathbf{p})$. These unknowns can be estimated by evaluating Eq. 11 at three different values of ψ. For instance, this can be achieved by taking three correlation measurements $B(\mathbf{p}, \psi)$ for $\psi = 0$, $\psi = \frac{2\pi}{3}$, and $\psi = \frac{4\pi}{3}$:

$$B(\mathbf{p}, 0) = o_b + a_b \cos\left(0 - \phi(\mathbf{p})\right) \tag{12}$$

$$B\left(\mathbf{p}, \frac{2\pi}{3}\right) = o_b + a_b \cos\left(\frac{2\pi}{3} - \phi(\mathbf{p})\right) \tag{13}$$

$$B\left(\mathbf{p}, \frac{4\pi}{3}\right) = o_b + a_b \cos\left(\frac{4\pi}{3} - \phi(\mathbf{p})\right). \tag{14}$$

For each measurement, the demodulation function $R(\psi, t)$ is shifted by phase ψ, and then correlated with the received radiance. This is shown in Figure 8. This process is called phase-shifting, and is similar to phase-shifting based active triangulation method described in the previous chapter (Section **??**). Whereas active triangulation method uses sinusoidal patterns that are spatially shifted, the time-of-flight approach discussed here uses temporally coded sinusoidal illumination.

The above set of equations can be written compactly as a linear system of three equations:

$$\mathbf{B} = \mathbf{C}\mathbf{X}, \tag{15}$$

where

$$\mathbf{B} = \begin{bmatrix} B(0) \\ B\left(\frac{2\pi}{3}\right) \\ B\left(\frac{4\pi}{3}\right) \end{bmatrix}, \quad \mathbf{C} = \begin{bmatrix} 1 & \cos(0) & \sin(0) \\ 1 & \cos\left(\frac{2\pi}{3}\right) & \sin\left(\frac{2\pi}{3}\right) \\ 1 & \cos\left(\frac{4\pi}{3}\right) & \sin\left(\frac{4\pi}{3}\right) \end{bmatrix}, \quad \mathbf{X} = \begin{bmatrix} o_b \\ a_b \cos(\phi) \\ a_c \sin(\phi) \end{bmatrix}. \tag{16}$$

of the sensor. Because of their low cost, CW ToF technique forms the basis of several consumer C-ToF devices [PMD-Technologies-gmbH ; Microsoft-Kinect ; Intel-SoftKinectic].

[7]Strictly speaking, the above equation is an approximation. It holds exactly only in the limit as the ratio $\frac{T_{int}}{T_{mod}}$ approaches infinity, where $T_{mod} = \frac{2\pi}{\omega}$ is the period of the modulation sinusoid. In practice, the approximation is valid since typically, T_{mod} is of the order of a few nanoseconds, and T_{int} is of the order of a few milliseconds. Also, the above equation gives the steady-state image brightness. It is the brightness value when the demodulation is performed after the system has reached a steady-state, that is after time $t > \tau$, when the light has reached the sensor after reflection from the scene.
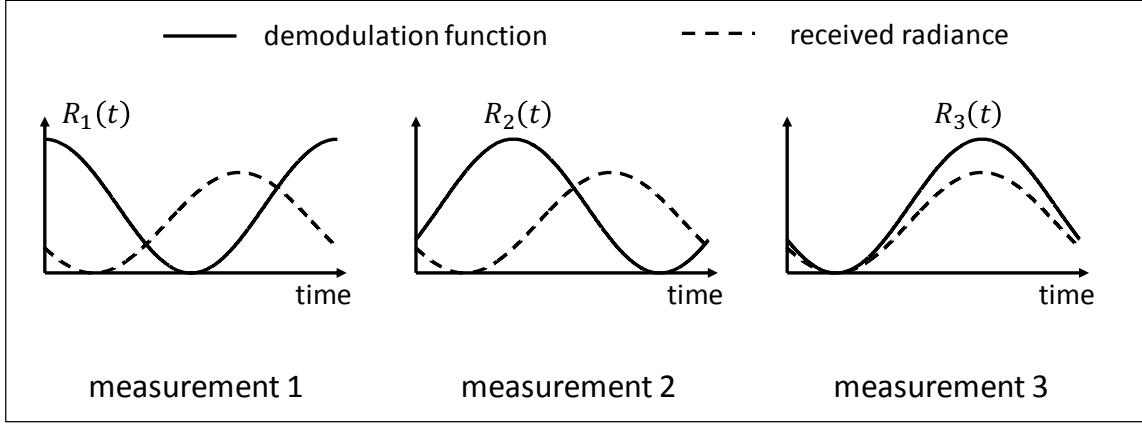
Fig. 8. Homodyne decoding. In homodyne decoding, both modulation and demodulation functions are sinusoids of the same frequency. Phase of the received light can be estimated by taking a minimum of three correlation measurements. For each measurement, the demodulation function is phase-shifted, and then correlated with the received radiance. This process is called phase-shifting, and is conceptually similar to phase-shifting based active triangulation methods.

For brevity, we have dropped the argument $\mathbf{p}$. $\mathbf{B}$ is the 3×1 vector of the measured intensities at pixel $\mathbf{p}$. $\mathbf{C}$ is called the measurement matrix; size of $\mathbf{C}$ is 3×3. $\mathbf{X}$ is the 3×1 unknown vector. $\mathbf{X}$ can be estimated by simple linear inversion: $\mathbf{X} = \mathbf{C}^{-1}\mathbf{B}$. Note that the linear inversion operator is performed for each camera pixel individually. Once $\mathbf{X}_{3\times1}$ is recovered, the phase ϕ is computed as:

$$\phi = \arccos\left(\frac{\mathbf{X}(2)}{\sqrt{\mathbf{X}(2)^2 + \mathbf{X}(3)^2}}\right) , \tag{17}$$

where $\mathbf{X}(j)$ is the jth, $j = [1, 2, 3]$ element of the estimated vector $\mathbf{X}_{3\times1}$. $\arccos(.)$ is the inverse cosine function [8]. Finally, the depth is computed as:

$$d = \frac{c\phi}{2\omega} . \tag{18}$$

---

[8] The function $\arccos(.)$ returns a phase value ϕ in the range of $[0, \pi]$. The true phase value could be either ϕ or $2\pi - \phi$. This is because $\cos(\theta) = \cos(2\pi - \theta)$. The two-way ambiguity can be resolved by considering the sign of $\mathbf{X}(2)$. If $\mathbf{X}(3) = a_c \sin(\phi) > 0$, then $0 \leq \phi \leq \pi$, else, $\pi \leq \phi \leq 2\pi$

3.2. The 4-Bucket Method

While three images are theoretically sufficient for estimating the phase, more measurements may be taken for increased robustness in the presence of large sensor noise. In general, we can take measurements $B(\mathbf{p}, \psi)$ at N different values of ψ. The phase-recovery process is similar to as described above, with the linear system being over-determined, which can be solved by using linear least squares methods.

One special case worth discussing is $N = 4$, i.e., taking four measurements at phase-shifts of $\frac{\pi}{2}$:

$$B\left(\mathbf{p}, 0\right) \;=\; o_b + a_b \cos\left(0 - \phi(\mathbf{p})\right) = o_b + a_b \cos\left(\phi(\mathbf{p})\right) \tag{19}$$

$$B\left(\mathbf{p}, \frac{\pi}{2}\right) \;=\; o_b + a_b \cos\left(\frac{\pi}{2} - \phi(\mathbf{p})\right) = o_b + a_b \sin\left(\phi(\mathbf{p})\right) \tag{20}$$

$$B\left(\mathbf{p}, \pi\right) \;=\; o_b + a_b \cos\left(\pi - \phi(\mathbf{p})\right) = o_b - a_b \cos\left(\phi(\mathbf{p})\right) \tag{21}$$

$$B\left(\mathbf{p}, \frac{3\pi}{2}\right) \;=\; o_b + a_b \cos\left(\frac{3\pi}{2} - \phi(\mathbf{p})\right) = o_b - a_b \sin\left(\phi(\mathbf{p})\right) . \tag{22}$$

From these measurements, the phase $\phi(\mathbf{p})$ can be recovered as:

$$\phi(\mathbf{p}) \;=\; \arctan\left(\frac{B\left(\mathbf{p}, \frac{\pi}{2}\right) - B\left(\mathbf{p}, \frac{3\pi}{2}\right)}{B\left(\mathbf{p}, 0\right) - B\left(\mathbf{p}, \pi\right)}\right) . \tag{23}$$

This method is used widely in several commercially available CW ToF sensors. In several hardware implementations, the four measurements are taken simultaneously using the 4-bucket (or 4-tap) lock-in pixel architecture [Lange et al. 2000], thus enabling *real-time* single-shot depth estimation.

3.3. Multi Frequency Phase Shifting

Image noise (e.g., photon noise) results in errors in the depth estimated using CW ToF systems. The depth error $\triangle d$ is inversely proportional to the modulation frequency ω [Lange and Seitz 2001]:

$$\triangle d \propto \frac{1}{\omega} . \tag{24}$$

Thus, higher the frequency used, higher the achieved depth accuracy. On the other hand, recall from Eq. 17 that the phase ϕ is computed by using inverse trigonometric functions (e.g., arctan, arcsine, arccosine), which have a range of 2π. Since the phase and the depth are related as $\phi = \omega \frac{2d}{c}$, the set of scene depths $d + n\frac{\pi c}{\omega}$ for any integer n will all have the same recovered phase, leading

to depth ambiguities. This is called the wrapped phase problem. It follows that the maximum depth range R_{max} in which depths can be measured unambiguously is given by $R_{max} = \frac{\pi c}{\omega}$ [Lange 2000]. For example, for $\omega = 2\pi \times 100$ MHz. [9], R_{max} is 1.5 meters.

This presents a tradeoff between achieving a large depth range, and achieving high depth accuracy. On one hand, higher modulation frequencies achieve high depth accuracy. On the other hand, using high frequencies results in a small unambiguous depth range, and a large number of possible depth ambiguities. How can we measure accurate scene depths in a large range?

It is possible to achieve both by using two or more frequencies [Payne et al. 2009; Jongenelen et al. 2010; Jongenelen et al. 2011]. The two frequencies could be such that one is sufficiently low to achieve the desired unambiguous depth range, and the other is sufficiently high to achieve the desired level of accuracy. The phase corresponding to the high frequency gives accurate, but ambiguous depth information. This is disambiguated using the noisy, but unambiguous phase corresponding to the low frequency. This hierarchical approach is similar to the multi-frequency methods used in spatial phase-shifting as discussed in the previous chapter (Section **??**). Alternatively, it is also possible to use multiple high frequencies [Jongenelen et al. 2010; Gupta et al. 2015]. For a detailed discussion on phase disambiguation (phase-unwrapping) methods in CW ToF imaging, see [Hansard et al. 2013].

3.4. Heterodyne Decoding

In CW ToF systems based on heterodyne decoding [Payne 1973; Smith 1980; Carnegie et al. 2005; Dorrington et al. 2007], the frequencies ω and ω' of the source modulation and sensor demodulation functions, respectively, are slightly different. This is shown in Figure 9 (a). Specifically, let $M(t)$ and $R(t)$ be given as:

$$M(t) = o_m + a_m \cos(\omega t) \tag{25}$$

$$R(\psi, t) = o_r + a_r \cos(\omega' t - \psi), \tag{26}$$

where o_m, a_m and ω are the offset, amplitude and frequency, respectively, of $M(t)$. o_r, a_r and ψ are the offset, amplitude and phase of $R(t)$. The frequencies ω and ω' are chosen so that $\omega_{beat} =$

---

[9]ω is the angular modulation frequency, which is 2π times the modulation frequency.
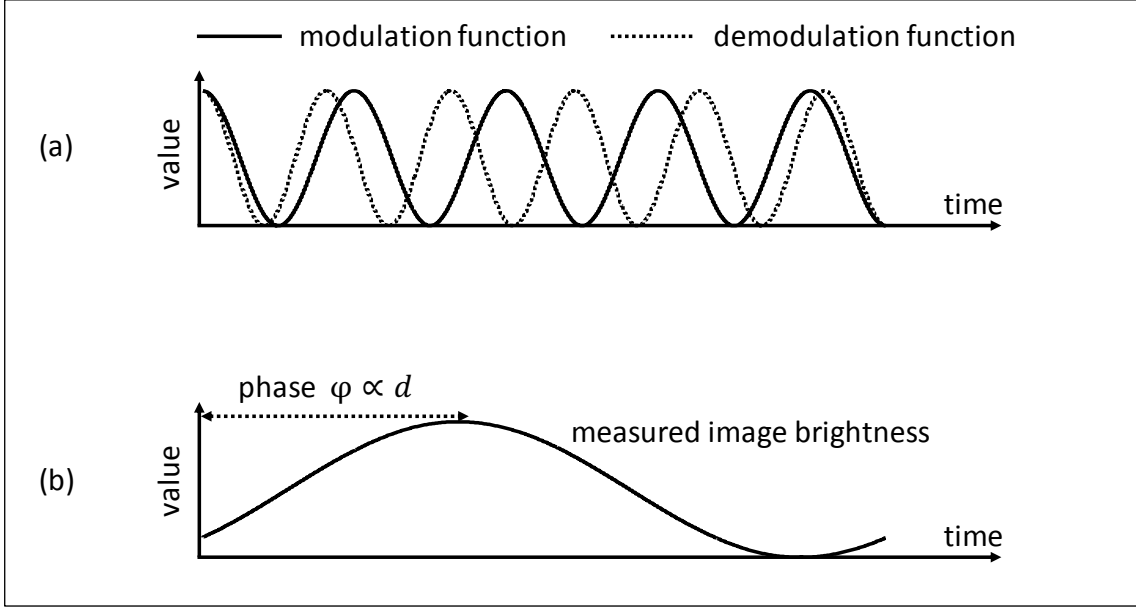
Fig. 9. **Heterodyne decoding.** (a) In CW ToF systems based on heterodyne decoding, the source modulation and sensor demodulation functions are sinusoids with different frequencies. The difference in the frequencies is called the beat frequency. (b) The captured image brightness varies sinusoidally as a function of the time instant when the measurement is taken. The frequency of the sinusoid is equal to the beat frequency. The phase can be recovered by taking three correlation measurements by either varying the phase of the demodulation function, or by taking measurements at different time instants.

$|\omega - \omega'| << \omega$ and $\omega_{beat} << \omega'$. For instance, typically, ω and ω' are of the order of $10 - 100$ MHz., whereas $\omega_{beat} = 0.1 - 1$ Hz.

As described in Eq. 8, the radiance $L(\mathbf{p}, t)$ incident at $\mathbf{p}$ is a scaled and phase-shifted version of $M(t)$. As in homodyne decoding, in order to measure the phase of $L(\mathbf{p}, t)$, it is correlated with the demodulation function $R(t)$. Substituting Eqs. 8 and 26 in Eq. 10, and simplifying, we get the expression for the measured brightness at a pixel $\mathbf{p}$ in heterodyne decoding:

$$B(\mathbf{p}, \psi, T) = o_b + a_b \cos\left(\omega_{beat} T + \psi - \phi(\mathbf{p})\right), \tag{27}$$

where o_b and a_b are as defined after Eq. 11 [10]. This equation is similar to the brightness equation (Eq. 11) for homodyne decoding, with one important difference. The image brightness in homo-

---

[10]We assume that $T_{beat} >> T_{int}$, where $T_{beat} = \frac{2\pi}{\omega_{beat}}$ is the period of the beat sinusoid. In practice, this approximation is valid becuase typically, $T_{beat} = 0.1 - 1$ seconds, and T_{int} is of the order of a few milliseconds.

dyne decoding is independent of the time instant T when the sensor takes the measurement [11]. In contrast, the image brightness in heterodyne decoding varies sinusoidally as a function of T with frequency equal to the beat frequency $\omega_{beat} = \omega' - \omega$. This is shown in Figure 9 (b).

Define $\psi' = \psi + \omega_{beat}T$. By substituting in Eq. 27, we get:

$$B(\mathbf{p}, \psi') = o_b + a_b \cos(\psi' - \phi(\mathbf{p})) . \tag{28}$$

This equation has the same form as Eq. 11. As in homodyne decoding, the phase $\phi(\mathbf{p})$ can be recovered by taking three correlation measurements $B(\mathbf{p}, \psi')$ for three different values of ψ', which can be achieved by either varying the phase ψ of the demodulation function, or by taking measurements at different time instants T. Note that if the latter method is used, sensor's integration periods must be synchronized temporally with the modulation and demodulation functions.

3.5. Noise And Error Analysis

The accuracy and resolution of a CW ToF system are limited by noise. There are several sources of noise, including shot (photon) noise, sensor read noise and quantization noise. Many of these sources are signal independent, and can be mitigated by using higher quality or cooled sensors. However, shot noise is due to the quantum nature of arriving photons and generated photo-electrons, and is thus present in every imaging system. Note that photon noise is due to photons of both the signal (light emitted from the source) and any background ambient illumination that is present in the scene. The standard deviation of photon noise is proportional to the square-root of the number of photons (optical shot noise) or photo-electrons (electronic shot noise) [Lange 2000; Hasinoff et al. 2010; Ratner and Schechner 2007; Schechner et al. 2007].

Due to its fundamental nature, shot noise places fundamental limits on the depth accuracy of a CW ToF system. The standard deviation of depth error $\triangle d$ of a CW ToF system that uses sinusoidal modulation is given by:

$$\triangle d = \frac{c\sqrt{o_b}}{\omega \kappa a_b}, \tag{29}$$

where ω is the modulation frequency [Lange and Seitz 2001]. o_b and a_b are the offset and amplitude of the demodulated brightness value received at a pixel (see Eq. 11). κ is a constant; it depends on the number of phase-shifts captured. More the number of images captured, higher the value of κ. The offset o_b is proportional to the amount of background illumination. Thus, stronger ambi-

---

[11]T is defined with respect to a reference time, e.g., the time instant when the light source starts emitting light.

ent illumination reduces the depth accuracy. The amplitude a_b is proportional to the light source strength, its modulation contrast (ratio of the amplitude and the offset of the emitted sinusoid) and the reflectance of the scene. Thus, the higher the light source power and the brighter the scene, higher the achieved depth accuracy.

Errors Due To Imperfect Modulation. Sinusoidal CW ToF systems assume that both the light modulation and the sensor demodulation (exposure) function are perfectly sinusoidal. However, in practice, the source and the sensor may be modulated by a digitally generated square wave signals. In that case, the modulation functions may have higher order harmonics, in addition to the base sinusoidal frequency. This results in systematic errors in the recovered depth. It is possible to mitigate these errors by reducing the duty cycle of the modulation waveforms [Payne et al. 2010]. It has been shown that if the modulation and demodulation signals are not perfectly sinusoidal, heterodyne systems achieve lower error rates as compared to homodyne systems [Dorrington et al. 2008; Conroy et al. 2009].

4. PSEUDO RANDOM BINARY CODING

In addition to sinusoids, several other waveforms have been used as modulation and demodulation functions in CW ToF imaging. Examples include square wave [Grootjans et al. 2006] and triangular wave [Ferriere et al. 2008]. One widely used waveform due to its ability to achieve high signal-to-noise ratio is the pseudo random binary sequence (PRBS) [Takeuchi et al. 1983; Takeuchi et al. 1986; Lee and Ramaswami 1992; Buxbaum et al. 2002; Grootjans et al. 2006]. The modulation and demodulation functions are both pseudo random binary sequences, for examples, M-sequences. These sequences were also discussed in the previous chapter in the context of designing single shot structured light patterns.

Consider a system that uses a temporal PRBS $prbs(t)$ as the modulation function:

$$M(t) = prbs(t) \,. \tag{30}$$

An example PRBS is shown in Figure 10 (a). As discussed previously in Section 3, the radiance $L(\mathbf{p}, t)$ incident at pixel $\mathbf{p}$ is a phase-shifted, scaled and offset version of $M(t)$:

$$L(\mathbf{p}, t) \;=\; \alpha(\mathbf{p}) \, prbs \, (t - \tau(\mathbf{p})) + A(\mathbf{p}) \,. \tag{31}$$

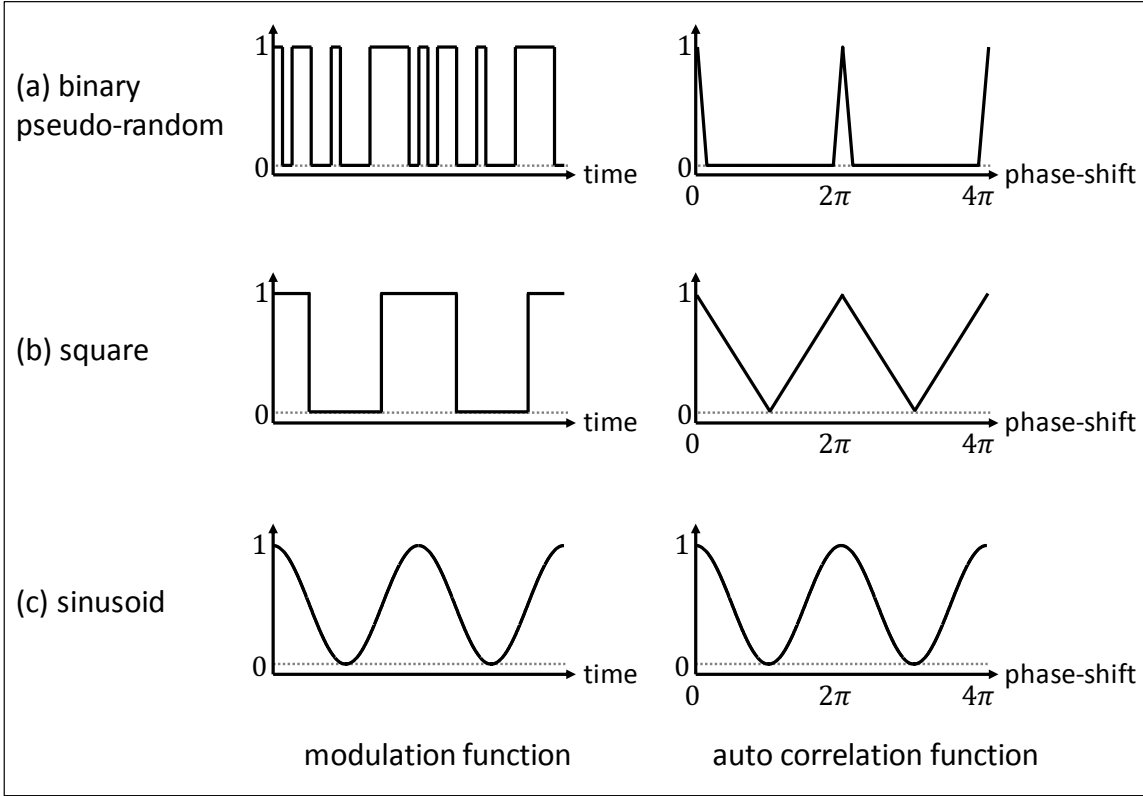Suppose the same PRBS is used as the demodulation function $R(t)$:

Fig. 10. **Different coding functions used in CW ToF and the corresponding auto-correlation functions.**

$$R(\psi, t) = prbs(t - \psi), \tag{32}$$

where ψ is the temporal shift between $R(t)$ and $M(t)$. Recall from Eq. 10 that the measured brightness at a pixel $\mathbf{p}$ is given by the correlation between $R(\psi, t)$ and $L(\mathbf{p}, t)$. Substituting Eqs. 31 and 32 in Eq. 10 and simplifying, we get:

$$B(\mathbf{p}, \psi) = o_b + a_b \, prbs(t - \tau(\mathbf{p})) \star prbs(t - \psi) \,. \tag{33}$$

where the offset and amplitude o_b and a_b were as defined previously in Section 3 after Eq. 11. Notice that the right hand side of the above equation contains an auto-correlation of the PRBS. The key property of PRBS is that their auto-correlation function is the delta (impulse) function. This is shown in Figure 10 (a). Thus, the above equation can be re-written as:

$$B(\mathbf{p}, \psi) = o_b + a_b \, \delta \left(\psi - \tau(\mathbf{p}) \right) \,. \tag{34}$$

The above equation states that the measured brightness values $B(\mathbf{p}, \psi)$ as a function of ψ have a peak at $\psi = \tau(\mathbf{p})$. Thus, the travel time (and hence the depth) at a pixel can be estimated by measuring $B(\mathbf{p}, \psi)$ at several different values of ψ, and identifying the location of the peak. The number of required brightness measurements is equal to the length of the binary code. For example, for an M-sequence of length 15 bits, 15 measurements will need to be captured.

Noise And Error Analysis. The auto-correlation function of PRBS is a delta function having a sharp well-defined peak. Thus, the process of depth estimation by peak identification is robust to noise [12]. In comparison, the auto correlation functions for sinusoidal and square waves are relatively smooth, as shown in Figure 10 (b-c). For a detailed discussion on the noise performance of pseudo random coding, see [Buttgen et al. 2007; Mitev et al. 2005; Ai et al. 2011].

Pseudo-random coding is also used to handle multi camera interference which arises when multiple ToF cameras are operating in a scene simultaneously [Buttgen et al. 2007]. Different cameras operate with different and mutually orthogonal pseudo-random M-sequences, thus minimizing the mutual interference.

5. CHIRP CODING

Chirp coding techniques were originally designed as alternatives to impulse-based RADAR methods [Hymans and Lait 1960; Griffiths 1990; Stove 1992] because of the latter's expensive hardware requirements. Later, the technique was adapted for range imaging LIDAR or LADAR systems [Stann et al. 1996; Bazin and Journet 1996; Collins et al. 1993; 1994].

Chirp coding uses CW modulation of the source. The modulation signal $M(t)$ (light emitted from the source) is a sinusoid whose frequency increases linearly with time. The instantaneous frequency $\omega(t)$ is given by:

$$\omega(t) = \omega_o + \frac{\triangle\omega}{T}\,t\,, \tag{35}$$

where ω_o is the initial frequency, $\triangle\omega$ is the difference between the final and the initial frequency, and T is the duration of the frequency sweep. Let the instantaneous phase of $M(t)$ be $\phi(t)$. $\phi(t)$ is given by integrating the instantaneous frequency over time:

---

[12] Modified M-sequences for achieving higher SNR have also been proposed [Lee and Ramaswami 1992; Emery and Flesia 1998].

$$\phi(t) \;=\; \int\limits_{0}^{t} \omega(t')dt' \,. \tag{36}$$

Substituting Eq. 35 into Eq. 36, and integrating, we get:

$$\phi(t) \;=\; \omega_o t + \frac{\triangle\omega t^2}{2T} \,. \tag{37}$$

The resulting function $M(t)$ is called a *chirp* signal, and is given by:

$$M(t) \;=\; o_m + a_m \cos\left(\phi(t)\right) \tag{38}$$

$$=\; o_m + a_m \cos\left(\omega_o t + \frac{\triangle\omega t^2}{2T}\right) \,, \tag{39}$$

where o_m and a_m are the constant offset and amplitude. An example chirp signal and its instantaneous frequency transform are illustrated in Figure 11 (a-b) (adapted from [Adany et al. 2009]).

As in the previous section, the received radiance $L(t)$ is given by scaling and time-shifting $M(t)$:

$$L(t) \;=\; o_l + a_l \cos\left(\omega_o\left(t - \tau\right) + \frac{\triangle\omega\left(t - \tau\right)^2}{2T}\right) \,, \tag{40}$$

where o_l and a_l are the offset and the amplitude of the received radiance, $\tau = \frac{2d}{c}$ is the time-shift (travel time), and d is the scene distance.

It can be shown that the frequency profile of $L(t)$ is a horizontally shifted version (along time dimension) of the frequency profile of $M(t)$. The amount of shift is equal to the travel time τ. This is shown in Figure 11 (c). Due to this time-shift, the instantaneous frequencies of $M(t)$ and $L(t)$ differ by a constant amount. The difference, ω_b, is proportional to the travel time τ (and the scene depth), as shown in Figure 11 (d):

$$\omega_b \;=\; \frac{\triangle\omega}{T}\tau \,. \tag{41}$$

Decoding Chirp For Computing Depth. Note that ω_b is the beat frequency of signals $M(t)$ and $L(t)$, and can be estimated by measuring their product. The multiplication is performed electrically by first converting $L(t)$ into an electrical signal $L_e(t)$ with a photo-diode sensor, and then mixing $L_e(t)$ with a copy of the original chirp signal $M(t)$ used to modulate the light source [Stann et al. 1996]. The product $P(t)$ is given as:

(a) modulation signal

(b) modulation signal

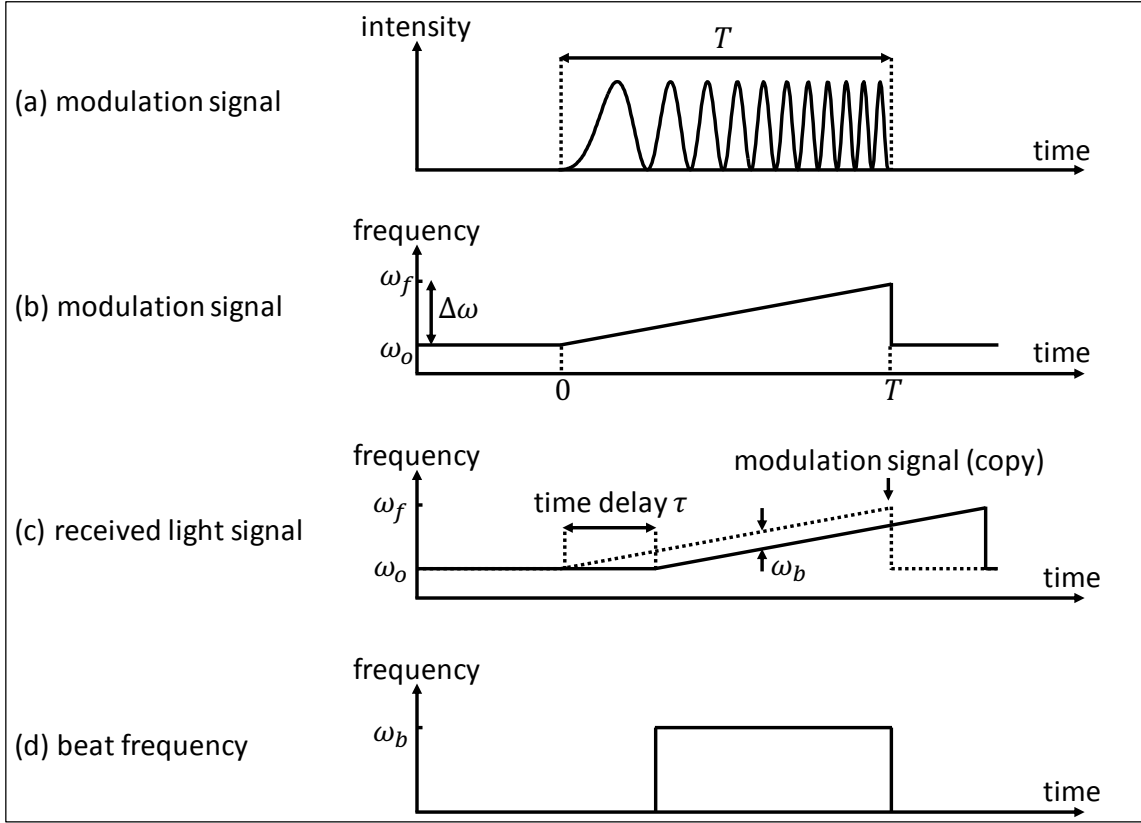(c) received light signal

(d) beat frequency

Fig. 11. **Chirp coding and decoding.** This figure is adapted from [Adany et al. 2009]. In chirp coding, the modulation signal is a sinusoid whose frequency increases linearly with time. (a) An example chirp modulation signal. (b) Instantaneous frequency transform of a chirp signal is a linear ramp. (c) The frequency transform of the radiance received at the sensor is a horizontally shifted version (along time dimension) of the frequency profile of the emitted modulation signal. (d) Due to this time-shift, the instantaneous frequencies of the modulation signal and the received light differ by a constant amount. The difference is proportional to the travel time (and the scene depth), and is measured by estimating the beat frequency of the modulation signal and the received light signal.

$$P(t) = L(t)M(t) \tag{42}$$

$$= o_p + a_p \cos\left(\frac{\triangle\omega\tau}{T}t + \omega_o\tau - \frac{\triangle\omega\tau^2}{2T}\right) + P_h(t), \tag{43}$$

where $o_p = o_m o_l$ and $a_p = \frac{a_m a_l}{2}$. The right hand side contains a DC term (o_p) and a temporal cosine term with frequency $\frac{\triangle\omega\tau}{T}$. The remaining terms are combined into the function $P_h(t)$. The frequency

of all the terms in $P_h(t)$ is greater than ω_o, the initial frequency. Chirp coding systems are designed so that $\omega_o > \frac{\triangle\omega\tau}{T}$. Since $P_h(t)$ contains only high frequency terms, it can be removed by low-pass filtering of $P(t)$. The filtered version, $P_f(t)$ is given by:

$$P_f(t) \;=\; o_p + a_p \cos\left(\frac{\triangle\omega\tau}{T}t + \omega_o\tau\right),\qquad(44)$$

where the τ^2 term is ignored, since typically, $\tau << T$. $P_f(t)$ is a temporal cosine function with frequency $\omega_b = \frac{\triangle\omega\tau}{T}$. The frequency ω_b can be estimated by computing the Fourier transform of $P_f(t)$. From the estimated frequency ω_b, the scene distance d can be computed as:

$$d \;=\; \frac{\omega_b T c}{2\triangle\omega}.\qquad(45)$$

5.1. Wavelength Modulated Chirp LIDAR

So far in this section, we have discussed systems where chirp coding is achieved by modulating the intensity of the emitted light. Chirp coding can also be performed by by modulating the wavelength of the emitted light [Zheng 2004; Strzelecki et al. 1988; Slotwinski et al. 1989; Beheim and Fritsch 1985; Dieckmann 1994; Amann et al. 2001; Nordin 2004]. This can be achieved by using tunable lasers whose optical frequency (wavelength) is modulated over time. The beat-frequency between the emitted and received signal is estimated by coherent detection.

The range resolution $\triangle d$ achieved by chirp coding based ToF system is inversely proportional to the frequency range [Stann et al. 1996]:

$$\triangle d \;=\; \frac{c}{2\triangle\omega}.\qquad(46)$$

If chirp coding is performed by wavelength modulation, the range of frequencies is significantly higher (hundreds of GHz.) as compared to what can be achieved by intensity modulated chirp coding (~ 100 MHz.). This can result in significantly higher range resolution. For details and analysis of optical frequency chirp coding, see [Zheng 2004].

5.2. Velocimetry Using Chirped LIDAR

Chirp based LIDARs have also been used to measure displacement [Beheim and Fritsch 1985] and velocity [Piracha et al. 2011; Nordin 2004]. While it is possible to measure velocity by estimating the

gradient of distance with respect to time, it is possible to measure the velocity directly by utilizing the Doppler effect (Doppler frequency shift) of moving objects.

Merits And Limitations Of Chirp Coding. Since chirp coding is a CW modulation method, it can be implemented with low-cost LEDs and laser diodes, since short high power pulses are not required. On the other hand, demodulation is performed by performing a frequency analysis on the received signal. This requires capturing a relatively large number of samples as compared to homodyne CW ToF method and thus, a large sensor bandwidth is needed. However, it is possible to reduce the sensor bandwidth requirement by multiplying the radiance received at the sensor with the modulation function optically (instead of electronically) before reaching the sensor [Adany et al. 2009].

REFERENCES

ADANY, P., ALLEN, C., AND HUI, R. 2009. Chirped lidar using simplified homodyne detection. *Journal of Lightwave Technology 27,* 16, 3351–3357.

ADMINISTRATION, N. O. A. US Interagency Elevation Inventory. http://coast.noaa.gov/inventory/.

AI, X., NOCK, R., RARITY, J. G., AND DAHNOUN, N. 2011. High-resolution random-modulation CW lidar. *Applied Optics 50,* 22.

AMANN, M.-C., BOSCH, T., LESCURE, M., MYLLYLA, R., AND RIOUX, M. 2001. Laser Ranging: A critical review of usual techniques for distance measurement. *Optical Engineering 40,* 1.

ANTHES, J. P., GARCIA, P., PIERCE, J. T., AND DRESSENDORFER, P. V. 1993. Nonscanned ladar imaging and applications. *Proc. SPIE 1936*, 11–22.

BAZIN, G. AND JOURNET, B. 1996. A new laser range-finder based on fmcw-like method. In *IEEE Instrumentation and Measurement Technology Conference*. Vol. 1. 90–93 vol.1.

BEHEIM, G. AND FRITSCH, K. 1985. Remote displacement measurements using a laser diode. *Electronics Letters 21,* 3, 93–94.

BUTTGEN, B., EL MECHAT, M.-A., LUSTENBERGER, F., AND SEITZ, P. 2007. Pseudonoise optical modulation for real-time 3-d imaging with minimum interference. *IEEE Transactions on Circuits and Systems I 54,* 10.

BUXBAUM, B., SCHWARTE, R., RINGBECK, T., GROTHOF, M., AND LUAN, X. 2002. Msm-pmd as correlation receiver in a new 3d-ranging system. *Proc. SPIE 4546*, 145–153.

CARNEGIE, D. A., CREE, M. J., AND DORRINGTON, A. A. 2005. A high-resolution full-field range imaging system. *Review of Scientific Instruments 76,* 8, 083702–7.

CARNEGIE, D. A., McCLYMONT, J. R. K., JONGENELEN, A. P. P., B. DRAYTO AND, A. A. D., AND PAYNE, A. D. 2011. Design and construction of a configurable full-field range imaging system for mobile robotic applications. *Lecture Notes in Electrical Engineering 83*.

COLLINS, S. F., HUANG, W. X., MURPHY, M. M., GRATTAN, K. T. V., AND PALMER, A. W. 1993. A simple laser diode ranging scheme using an intensity modulated fmcw approach. *Measurement Science and Technology 4,* 12.

COLLINS, S. F., HUANG, W. X., MURPHY, M. M., GRATTAN, K. T. V., AND PALMER, A. W. 1994. Ranging measurements over a 20 metre path using an intensity-chirped laser diode. *Measurement Science and Technology 5,* 6.

CONROY, R. M., DORRINGTON, A. A., KNNEMEYER, R., AND CREE, M. J. 2009. Range imager performance comparison in homodyne and heterodyne operating modes. *Proc. SPIE 7239*, 723905–10.

COVA, S., LONGONI, A., AND ANDREONI, A. 1981. Towards picosecond resolution with single-photon avalanche diodes. *Review of Scientific Instruments 52,* 3, 408–412.

DIECKMANN, A. 1994. FMCW-LIDAR with tunable twin-guide laser diode. *Electronics Letters 30,* 4, 308–309.

DORRINGTON, A. A., CREE, M. J., CARNEGIE, D. A., PAYNE, A. D., CONROY, R. M., GODBAZ, J. P., AND JONGENELEN, A. P. P. 2008. Video-rate or high-precision: A flexible range imaging camera. In *Proc. SPIE (6813).*

DORRINGTON, A. A., CREE, M. J., PAYNE, A. D., CONROY, R. M., AND CARNEGIE, D. A. 2007. Achieving sub-millimetre precision with a solid-state full-field heterodyning range imaging camera. *Measurement Science and Technology 18,* 9.

EMERY, Y. AND FLESIA, C. 1998. Use of the a1- and the a2-sequences to modulate continuous-wave pseudorandom noise lidar. *Appl. Opt. 37,* 12, 2238–2241.

EVENSON, K. M., WELLS, J. S., PETERSEN, F. R., DANIELSON, B. L., DAY, G. W., BARGER, R. L., AND HALL, J. L. 1972. Speed of light from direct frequency and wavelength measurements of the methane-stabilized laser. *Phys. Rev. Lett. 29*, 1346–1349.

FERRIERE, R., CUSSEY, J., AND DUDLEY, J. 2008. Time-of-flight range detection using lowfrequency intensity modulation of a cw laser diode: Application to fiber length measurement. *Optical Engineering 47,* 9.

GRIFFITHS, H. D. 1990. New ideas in FM radar. *Electronics Communication Engineering Journal 2,* 5, 185–194.

GROOTJANS, R., DER TEMPEL, W. V., NIEUWENHOVEC, D. V., DE TANDT, C., AND KUIJK, M. 2006. Improved modulation techniques for time-of-flight ranging cameras using pseudo random binary sequences. In *Proc. IEEE LEOS Benelux Chapter.*

GUPTA, M., NAYAR, S. K., HULLIN, M., AND MARTIN, J. 2015. Phasor Imaging: A Generalization of Correlation Based Time-of-Flight Imaging. *ACM Transactions on Graphics.*

HANSARD, M., LEE, S., CHOI, O., AND HORAUD, R. 2013. Disambiguation of time-of-flight data. In *Time-of-Flight Cameras.* Springer Briefs in Computer Science. 29–43.

HASINOFF, S., DURAND, F., AND FREEMAN, W. 2010. Noise-optimal capture for high dynamic range photography. In *IEEE Conference on Computer Vision and Pattern Recognition (CVPR).* 553–560.

HYMANS, A. AND LAIT, J. 1960. Analysis of a frequency-modulated continuous-wave ranging system. *Proceedings of the IEE - Part B: Electronic and Communication Engineering 107,* 34, 365–372.

INTEL-SOFTKINECTIC. http://www.engadget.com/2013/06/04/intel-announces-creative-depth-vision-camera-at-computex-2013/.

JONGENELEN, A. P. P., BAILEY, D. G., PAYNE, A. D., DORRINGTON, A. A., AND CARNEGIE, D. A. 2011. Analysis of errors in tof range imaging with dual-frequency modulation. *IEEE Transactions on Instrumentation and Measurement 60,* 5.

JONGENELEN, A. P. P., CARNEGIE, D., PAYNE, A., AND DORRINGTON, A. 2010. Maximizing precision over extended unambiguous range for tof range imaging systems. In *IEEE Instrumentation and Measurement Technology Conference (I2MTC).*

KILPELA, A. 2004. Pulsed time-of-flight laser range finder techniques for fast, high precision measurement applications. *PhD Thesis, Dept. of Electronics, University of Oulu.*

KIRMANI, A., HUTCHISON, T., DAVIS, J., AND RASKAR, R. 2009. Looking around the corner using transient imaging. In *IEEE ICCV.*

KOECHNER, W. 1968. Optical ranging system employing a high power injection laser diode. *IEEE Trans. aerospace and electronic systems 4,* 1.

LANGE, R. 2000. 3d time-of-flight distance measurement with custom solid-state image sensors in cmos-ccd-technology. *PhD Thesis*.

LANGE, R. AND SEITZ, P. 2001. Solid-state time-of-flight range camera. *IEEE J. Quantum Electronics 37,* 3.

LANGE, R., SEITZ, P., BIBER, A., AND LAUXTERMANN, S. 2000. Demodulation pixels in ccd and cmos technologies for time-of-flight ranging. In *IST/SPIE International Symposium on Electronic Imaging*.

LEE, H. S. AND RAMASWAMI, R. 1992. Study of pseudo-noise cw diode laser for ranging applications. *Proc. SPIE 1829*, 36–45.

LEICA-GEOSYSTEMS. Pulsed LIDAR Sensor. http://www.leica-geosystems.us/en/index.htm.

MAMON, G., YOUMANS, D. G., SZTANKAY, Z. G., AND MONGAN, C. E. 1978. Pulsed gaas laser terrain profiler. *Appl. Opt. 17,* 6, 868–877.

MASSA, J. S., BULLER, G. S., WALKER, A. C., COVA, S., UMASUTHAN, M., AND WALLACE, A. M. 1998. Time-of-flight optical ranging system based on time-correlated single-photon counting. *Appl. Opt. 37,* 31, 7298–7304.

MICROSOFT-KINECT. http://news.xbox.com/2014/04/xbox-one-march-npd.

MITEV, V., MATTHEY, R., DO CARMO, J. P., AND ULBRICH, G. 2005. Signal-to-noise ratio of pseudo-random noise continuous wave backscatter lidar with analog detection. *Proc. SPIE 5984*.

MORING, I., HEIKKINEN, T., MYLLYLA, R., AND KILPELA, A. 1989. Acquisition of three-dimensional image data by a scanning laser range finder. *Optical Engineering 28,* 8.

NICLASS, C., ROCHAS, A., BESSE, P.-A., AND CHARBON, E. 2005. Design and characterization of a CMOS 3-D image sensor based on single photon avalanche diodes. *IEEE Journal of Solid-State Circuits 40,* 9, 1847–1854.

NORDIN, D. 2004. Optical Frequency Modulated Continuous Wave (FMCW) Range and Velocity Measurements. *PhD Thesis, Dept. of Computer Science and Electrical Engineering, Lulea University of Technology*.

PANDHARKAR, R., VELTEN, A., BARDAGJY, A., LAWSON, E., BAWENDI, M., AND RASKAR, R. 2011. Estimating motion and size of moving non-line-of-sight objects in cluttered environments. In *IEEE Conference on Computer Vision and Pattern Recognition*. 265–272.

PAYNE, A. D., DORRINGTON, A. A., AND CREE, M. J. 2010. Illumination waveform optimization for time-of-flight range imaging cameras. In *Proc. SPIE 8085*.

PAYNE, A. D., JONGENELEN, A. P., DORRINGTON, A. A., CREE, M. J., AND CARNEGIE, D. A. 2009. Multiple frequency range imaging to remove measurement ambiguity. In *Proc. of Conference on Optical 3-D Measurement Techniques*.

PAYNE, J. M. 1973. An optical distance measuring instrument. *Review of Scientific Instruments 44,* 3, 304–306.

PIRACHA, M. U., NGUYEN, D., OZDUR, I., AND DELFYETT, P. J. 2011. Simultaneous ranging and velocimetry of fast moving targets using oppositely chirped pulses from a mode-locked laser. *Opt. Express 19,* 12, 11213–11219.

PMD-TECHNOLOGIES-GMBH. Photonic mixer devices. http://www.pmdtec.com/.

RATNER, N. AND SCHECHNER, Y. 2007. Illumination multiplexing within fundamental limits. In *IEEE Conference on Computer Vision and Pattern Recognition*. 1–8.

SCHECHNER, Y. Y., NAYAR, S. K., AND BELHUMEUR, P. N. 2007. Multiplexing for optimal lighting. *IEEE Trans. Pattern Anal. Mach. Intell. 29,* 8, 1339–1354.

SCHWARTE, R., XU, Z., HEINOL, H., OLK, J., KLEIN, R., BUXBAUM, B., FISCHER, H., AND SCHULTE, J. 1997. New electro-optical mixing and correlating sensor: Facilities and applications of the photonic mixer device. In *Proc. SPIE (3100)*.

SLOTWINSKI, A. R., GOODWIN, F. E., AND SIMONSON, D. L. 1989. Utilizing GaAlAs Laser Diodes As A Source For Frequency Modulated Continuous Wave (FMCW) Coherent Laser Radars. *Proc. SPIE 1043*, 245–251.

SMITH, D. E. 1980. Electronic distance measurement for industrial and scientific applications. *Hewlett-Packard Journal 31,* 6.

STANN, B. L., RUFF, W. C., AND SZTANKAY, Z. G. 1996. Intensity-modulated diode laser radar using frequency-modulation/continuous-wave ranging techniques. *Optical Engineering 35,* 11, 3270–3278.

STOVE, A. G. 1992. Linear fmcw radar techniques. *IEEE Proceedings of Radar and Signal Processing 139,* 5, 343–350.

STRZELECKI, E. M., COHEN, D. A., AND COLDREN, L. A. 1988. Investigation of tunable single frequency diode lasers for sensor applications. *Journal of Lightwave Technology 6,* 10, 1610–1618.

TAKEUCHI, N., BABA, H., SAKURAI, K., AND UENO, T. 1986. Diode-laser random-modulation cw lidar. *Appl. Opt. 25,* 1, 63–67.

TAKEUCHI, N., SUGIMOTO, N., BABA, H., AND SAKURAI, K. 1983. Random modulation cw lidar. *Appl. Opt. 22,* 9, 1382–1386.

VELODYNE. Pulsed LIDAR Sensor. http://www.velodynelidar.com/lidar/lidar.aspx.

VELTEN, A., WILLWACHER, T., GUPTA, O., VEERARAGHAVAN, A., BAWENDI, M. G., AND RASKAR, R. 2012. Recovering three-dimensional shape around a corner using ultrafast time-of-flight imaging. *Nature 3 (745)*.

ZHENG, J. 2004. Analysis of optical frequency-modulated continuous-wave interference. *Appl. Opt. 43,* 21, 4189–4198.